Acta Biomaterialia 141 (2022) 466–480

Contents lists available at ScienceDirect

Acta Biomaterialia

journal homepage: www.elsevier.com/locate/actbio

Full length article

Insights into tribofilm formation on Ti-6V-4Al in a bioactive environment: Correlation between surface modification and micro-mechanical properties

J. Qi[a], D. Guan[a], J. Nutter[a], B. Wang[b], W.M. Rainforth[a,*]

[a] Department of Materials Science and Engineering, The University of Sheffield, Sheffield S1 3JD, UK
[b] Department of Mechanical Engineering Sciences, University of Surrey, Guildford, GU2 7XH, UK

ARTICLE INFO

Article history:
Received 22 September 2021
Revised 16 December 2021
Accepted 14 January 2022
Available online 19 January 2022

Keywords:
Tribofilm
Carbon nano onion (CNO)
EELS
Geometrically necessary dislocations (GND)
Precession electron diffraction (PET)
Tribocorrosion

ABSTRACT

Ti-6Al-4V has been used as a surgical implant material for a long time because of its combination of strength, corrosion resistance and biocompatibility. However, there remains much that is not understood about how the surface reacts with the environment under tribocorrosion conditions. In particular, the conditions under which tribofilms form and their role on friction and wear are not clear. To evaluate the complicated nature of the dynamic surface microstructural changes on the wear track, high resolution transmission electron microscopy (TEM), scanning transmission electron microscope (STEM) and electron energy loss spectroscopy (EELS) have been used to characterise the structure and chemical composition of the tribofilm. Detailed analysis of the formation and structure of the tribofilm and the metal surface deformation behaviour were studied as a function of applied potential and the role of proteins in the lubricant. For the first time, graphitic and onion-like carbon structures from wear debris were found in the testing solution. The presence of carbon nanostructures in the tribocorrosion process and the formation of the tribofilm leads to an improved tribocorrosion behaviour of the system, in particular a reduction in wear and friction. A detailed, quantitative, analysis of surface deformation was undertaken, in particular, the geometrically necessary dislocation (GND) density was quantified using precession electron diffraction (PET). A clear correlation between applied potential, tribofilm formation and the surface strain was established.

Statement of significance

The formation of tribofilm and microstructure modification of the Ti-6Al-4V surface during tribocorrosion in a physiological environment is not fully understood. In particular, the correlation between microstructural changes and electrochemical conditions is not clear. This study presents a detailed investigation of the structure and chemical composition of tribofilms at the nanoscale during tribocorrosion tests in simulated body fluid and gives a detailed and quantitative description of the evolved surface structure. A clear correlation between applied potential, tribofilm formation and the surface strain was established. Moreover, particular attention is paid to the wear debris particles captured from the lubricating solution, including nanocarbon onion structures. The implications for tribocorrosion of the alloy in its performance as an implant are discussed.

1. Introduction

Ti-6Al-4V, with predominantly a hexagonal close packed (hcp) α-phase and a small fraction of body centred cubic (bcc) β-phase, has been extensively used for biomedical applications such as dental implants, bone anchorage of extra-oral prostheses, bone fixation systems and orthopaedic devices due to its biocompatibility and high corrosion resistance [1]. Ti-6Al-4V readily forms a thin, dense, titanium oxide layer on the surface which enhances the corrosion resistance in physiological environments [2]. However, the physiological environment varies with the specific application of the device and the host's health condition, for example peri-implant inflammation and as a direct consequence of the deterioration of the implant itself [3,4].

* Corresponding author.
E-mail address: m.rainforth@sheffield.ac.uk (W.M. Rainforth).

https://doi.org/10.1016/j.actbio.2022.01.027

Adverse local tissue and possible systemic reactions and toxicities resulting from the wear and corrosion products associated with metal implants have been widely reported [4–10]. Many *in vivo* studies have shown the existence of particles/debris of different sizes in peri-implant tissues around the implant alloys in the case of both Ti and CoCr alloys [4–8]. Inflammation around the peri-implant tissue generates reactive oxygen species (ROS) (H_2O_2, $HClO_4^-$ *etc.*) to kill the bacterial infection. However, ROS can drastically alter or even increase corrosion by damaging the oxide film and the potential of the solution is raised [4,9]. It is, therefore, important to differentiate the impact on implant degradation of ROS oxidation (affecting corrosion) from the alteration of the solution potential to provide additional insight into how the system reacts under tribocorrosive environments with varying potentials.

Tribocorrosion plays a decisive role in implant degradation in the human body where two metal components are in contact, or a metal component is in contact with another surface such as a bone, ceramic or cement. There are three interrelated components: tribology (friction, wear and lubrication), corrosion (material and its environment) and biochemistry (interaction between cells and protein) [11]. To understand these issues, tribocorrosion test methods have been developed over the years under well-defined loading and sliding conditions [12]. The absorption of protein (albumin for example) onto the Ti alloy implant surface has been investigated in conditions where there is no contact to disturb the surface and has clearly shown that protein absorption is an important part of the processes [13–17]. Analysis and characterisation of the chemical composition and structure of a tribofilm, as well as its role in tribocorrosion processes, are key to explaining the materials performance [18–21]. Reports on the structure of the tribofilm vary. Liao et al. [22] reported a graphitic tribofilm in metal-on-metal hip (CoCrMo) replacements retrieved from patients. In contrast, Zheng et al. [23] found an amorphous carbonaceous top layer up to 500 nm thick on the surface of a CoCrMo alloy that had also developed a nanocrystalline subsurface structure. Similarly, Hesketh et al. [24] reported an amorphous tribofilm with no long-range graphitic ordering. Balachandran et al. [25] recently reported the microstructure and compositional alterations in the subsurface of Ti-6Al-4V and CoCrMo alloy couple during fretting and showed the complexity of the surface changes. Clearly, a better understanding of the surface structural changes and the formation of tribofilms is needed.

Tribological contact often leads to surface deformation which is known to change the behaviour of the material to the local environment [18,26]. Perret et al. [20] and Maldonado et al. [21] have shown that the deformation of the material underneath the rubbed surface depends on the local electrochemical conditions prevailing during tribocorrosion. The reasons for this are far from fully understood.

Surface deformation leads to a substantial increase in dislocation density and often a considerable refinement in the microstructural scale, the extent of which depends on surface-specific strain hardening behaviour. Conventional TEM allows some of this information to be acquired, but diffraction information is usually averaged over a significant length scale. Precession electron diffraction (PED) is a recent technique in the TEM to fully quantify fine-scale deformation structure in terms of phase constitution, nanoscale misorientation and the dislocation density. PED offers a spatial resolution of 0.5-5 nm, with an outstanding angular resolution of ~0.1° [27]. The technique has been used extensively to investigate the deformed structure in adiabatic shear bands of titanium alloy [28], the deformation structures in ultrafine-grained titanium [29] and the defect structure of nano-scaled non-ferrous structural alloys [27,30]. However, using PED to characterise nanocrystalline deformation structures generated by tribological contact has not yet been reported and is implemented here for the first time.

It is clear that the formation of the tribofilm and the microstructure modification of the surface of the Ti-6Al-4V during tribocorrosion in a physiological environment is not fully understood. In particular, microstructural changes are not understood as a function of critical variables such as electrochemical conditions. This study presents a detailed investigation of the structure and chemical properties of tribofilms and surface structure formed at nanoscale during tribocorrosion tests in simulated body fluid. The micromechanical properties of these features are fully characterised, giving the first quantitative description of the evolved surface structure. Moreover, particular attention is paid to the wear debris particles captured from the lubricating solution, including nanocarbon onion structures. The implications for tribocorrosion of the alloy in its performance as an implant are discussed.

2. Experimental

2.1. Materials

Commercially available grade 5 Ti-6Al-4V ELI (Extra Low Interstitial) alloy from Ti-shop (UK) for surgical implant applications (specification ASTM F136) was used in this study. The Ti-6Al-4V alloy sheet with a thickness of 3 mm was sectioned by wire electrical discharge machining (WEDM) into 22 × 22 mm square coupons and mechanically ground and polished to a 0.25 µm silica suspension finish. The polished coupons were then cleaned by sonication in deionised water and isopropanol for 20 minutes before each tribocorrosion test.

25 vol. % Bovine Serum Albumin (BSA) (First Link Ltd., UK) in phosphate-buffered saline (PBS) (Sigma - Aldrich) solution was used as the simulated body fluid solution. This gives a solution with a protein content of 15.8 g/L, which is within the range of normal protein content in the human body fluid of a healthy human. Ultrapure water (Alfa Aesar) was used for preparing the solution and cleaning/rinsing surfaces. The initial pH of the solution was 7.45 and the end value was 7.01.

2.2. Tribocorrosion test procedure

A ball on disk reciprocating sliding configuration, which conformed to ASTM G133, was used. Inert 4 mm diameter Al_2O_3 balls (99.0%, Oakwade Ltd., UK) were used as the counter-body. The tribocorrosion tests were carried out in a three-electrode tribocorrosion cell on a Universal Micro Tribometer (UMT) TriboLab (Bruker) integrated with an EasyStat potentiostat. The reference electrode (RE) was Ag/AgCl, with a platinum wire as the counter electrode (CE) and the Ti-6Al-4V coupon was the working electrode (WE). An applied normal load of 0.5 N was selected, which gave a nominal initial Hertzian contact pressure of 600 MPa, assuming elastic contact conditions. The reciprocating stroke length was 2 mm, and the sliding speed was 20 mm/s. The latent time (the time between two successive contact events) was 0.1 s. Various testing times up to 4.5 hours were used, which gave a total sliding distance of 3240 m.

The first set of two tests were conducted under Open Circuit Potential (OCP) conditions. Cleaned Ti-6Al-4V coupons were mounted into the tribo-corrosion cell and initially slid against the 4 mm Al_2O_3 ball in the PBS solution for one hour. Diluted BSA solution (37°C) was then added in one of the tests without stopping the sliding. The final concentration of BSA in this test solution was 25 vol. %. The other one continued sliding in PBS solution. Both tests were stopped after another 2 hours of sliding.

Secondly, the tribocorrosion behaviour of Ti-6Al-4V was investigated at different surface potentials, namely at +0.5V, -0.5V, -0.8V and -0.95V. These were selected on the basis of an extensive study into the effect of applied potential on the surface oxide behaviour

in the same alloy investigated here [31]. These potentials are also consistent with the work of Hsu et al. [32], who examined the corrosion behaviour of Ti-6Al-4V by electrochemical techniques. In this series of tests, BSA was added to make a 25 vol. % solution from the beginning of the test. Load and sliding were applied after a 30 min wait to allow the system to stabilise. The set potential was applied simultaneously at the onset of the tribocorrosion tests. All the potential values reported in this work were measured against the Ag/AgCl reference electrode. Tests under each condition were repeated at least three times, with the data presented representative of the three tests. Data was compressed, and the COF was processed by an oscillating function using 50% in the middle of each motion by Viewer software (UMT, Bruker).

2.3. Analysis and characterisation of the worn surface and particles from the testing solution

After the tribocorrosion test, all the samples were rinsed briefly by ultrapure water then left to dry under air for post-test analysis. The profiles of the wear scars and wear volumes were measured and calculated using a Bruker Alicona surface profiler. The specific wear rate K, with units in $mm^3/N/m$ was calculated by the standard formula:

$$K = \frac{V}{dL}$$

where V is the wear volume of material loss in mm^3, L is the normal load in N and d is the total sliding distance in m.

The test solution was transferred into a clean centrifuge tube and kept still for 20 minutes. Then the top supernatant was taken for preparing the TEM samples for examining the wear debris/nanoparticles in the test solutions by following the standard procedure. TEM grids with silicon monoxide support film were used to prepare the TEM samples of tribological debris from the testing solutions.

The morphology and composition of the tribofilm on the wear scars were observed using an FEI F50 Scanning Electron Microscopy (SEM) with Energy-dispersive X-ray spectroscopy (EDX) system, operating at 1 kV (secondary electron images), 2 kV (backscattered electron image) and 15 kV(EDX).

2.4. Analysis and characterisation of microstructure of subsurface

The cross-sectional samples for tribofilm and subsurface analysis and characterisation were prepared by FIB following standard procedures using the FEI Helios Nanolab G3 with a Ga^+ ion source operated at 30 kV. The structure and chemical composition of the interface, tribofilm and the subsurface were examined using a cold field emission gun (c-FEG) JEOL F200 TEM coupled with a twin, solid-state, ultra-sensitive large silicon drift detectors (SDD) EDX system operating at 200 kV.

Precession electron diffraction (PET) using the NanoMegas STAR^{TM} PET and ASTAR^{TM} ACOM-TEM systems integrated into the JEOL F200 TEM was used to acquire the orientation data for the calculation of the geometrically necessary dislocation (GND) density. A precession angle of 1.4° was configured for all experiments. The precession frequency was 100 Hz and a beam spot size of 2 nm was used. A step size of 7 nm for both x and y directions was used for the OCP and -0.95V samples and 2 nm for the +0.5V and PBS only samples. The diffraction patterns were collected at a camera length of 150 nm. Once collected, the dataset was matched against diffraction patterns in the database and indexed automatically by Index software (NanoMegas, Belgium). The data was then exported and post-processed by the customised MATLAB scripts (originally from MTEX [33]) to calculate the grain boundary (GB) and GND density.

2.5. Statistical analysis

The Shapiro-Wilk test was used to assess the normality of the distribution of wear rate. Results are presented as mean ± standard deviation. All wear rates in this study were distributed normally. Differences and sample means were tested and compared by one-way ANOVA and Tukey comparison test to determine if the wear rate of each condition differed from one another. The values $P < 0.05$ were considered statistically significant.

Nonparametric statistical tests were used for examining the grain size and GND density distribution because their normality of distribution cannot be assumed. The data sets from the four testing conditions are treated as independent samples. The Kruskal-Wallis ANOVA method was used to assess the differences and sample means of grain size and GND density of each testing condition. The differences in GND density have been tested for each selected slip system, and the values $p < 0.01$ were considered statistically significant. Statistical analysis was performed on OriginPro® 2020b 9.7.5.184 (Academic) (OriginLab Corporation, Massachusetts, USA).

3. Results

3.1. Tribocorrosion behaviour in simulated body fluid

3.1.1. Tribocorrosion behaviour with and without BSA

To show the impact of BSA on the tribocorrion process, tribocorrosion tests in solutions with and without BSA were performed. Both sets of tests (Fig. 1) started in the PBS solutions without BSA. This was to ensure that running-in was complete and the sliding couple was operating in steady state. Then after one hour of sliding, the BSA was added into one of the tests (Fig. 1A), while the other continued sliding in PBS buffer solution alone (Fig. 1B). The total sliding time for both tests was 3 hours. In the PBS only solution, the friction (red line) exhibited a continuous rise from of 0.32 - 0.48 at the start of the test to 0.42-0.8 after 3h, with an increasingly noisy signal. In contrast, when the BSA was added after 1h sliding (Fig. 1A) the COF suddenly dropped from 0.32 - 0.48 to 0.28 - 0.38 with less noise than experienced in the first hour. After about another 40 minutes sliding, the COF abruptly became smooth. The noise in the COF curve remained low until the end of the test, although there were brief periods where the COF oscillated more strongly.

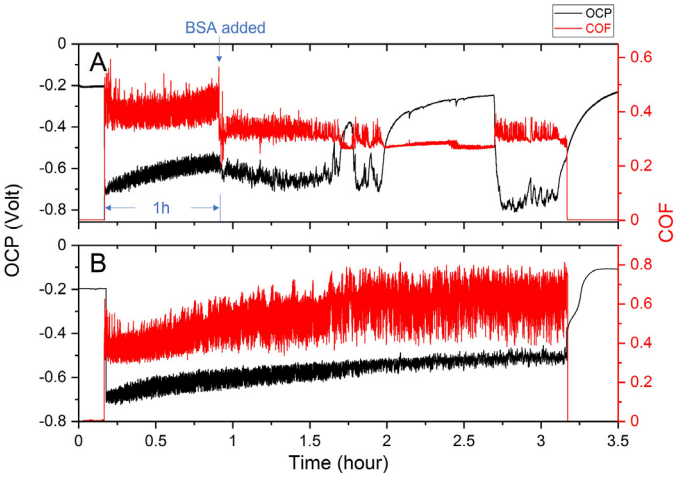

Fig. 1. Tribocorrosion measurements for Ti-6Al-4V sliding against Al_2O_3 in A) 25 vol.% BSA in PSA buffer simulated body fluid. BSA was added after 1 hour of sliding in PBS solution with continued sliding for another 2 hours, and B) PBS buffer solution alone.

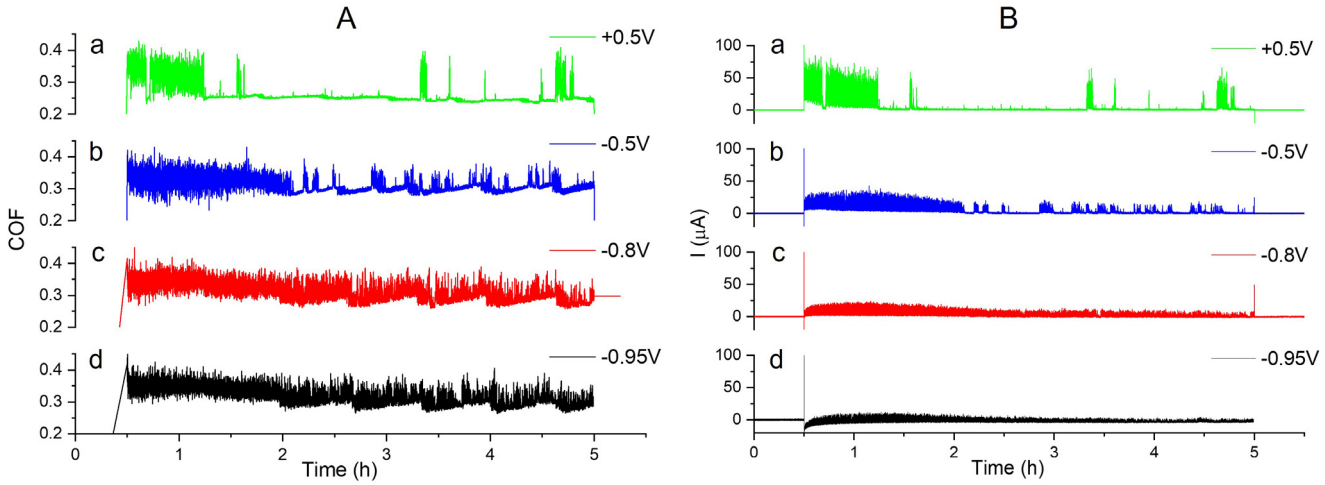

Fig. 2. Tribocorrosion behaviour A) COFs and B) currents at different applied potentials. (a) E = +0.5V; (b) E = -0.5V; (c) E = -0.8V; (d) E = -0.95V. Sliding was undertaken for 4.5 hours for all tests after a 30 min stabilisation time.

In both tests, at the initial running-in stage in the PBS only solution, the potential (black line) dropped from approximately -0.2V to -0.7V, then stabilised around at -0.6V at the end of one-hour sliding. After the addition of BSA (Fig. 1A), the potential decreased to -0.65V and gradually decreased with further sliding. Then, after another ~40 min sliding, there was an abrupt rise in the OCP to -0.39V, which coincided with the drop in the COF (both in value and the extent of noise). After a period of further stable behaviour, there was an abrupt drop to -0.71V, which coincided with the onset of noise in the COF. The OCP then rose to -0.25V, again associated with a period of stable COF. There was then an abrupt drop to -0.82V, again associated with the onset of noise in the COF. Thus, drops in the OCP appeared to be associated with stable periods of the COF, while abrupt rises in the OCP were associated with significant noise in the COF curve. The increase in the OCP is expected to be associated with the formation of a protection layer resulting in surface passivation, which clearly resulted in a lower, more stable COF. However, the abrupt reductions would have been associated with a break-up of the passive surface film, associated with an unstable COF. In contrast, in the test without the addition of BSA (Fig. 1B) after initial running-in, the OCP slowly increased from -0.7V to approximately -0.5V at the end of 3-hour sliding, with the noise in the potential signal decreasing as the test proceeded. There was no abrupt change in either OCP or COF during the whole process. Clearly, as Fig. 1 shows, there was a dynamic process with repeated breakdown and recovery of the passive surface film with the addition of BSA.

The friction and corrosion performance improved after the addition of BSA, but obviously there was an incubation time before the COF and OCP became stable. Thus, the addition of BSA clearly helped the formation of a surface protective layer. Numerous studies have shown that dissolved proteins affect the friction and wear performance of metal-on-metal and metal-on-polymer components [34].

3.1.2. Tribocorrosion behaviour with different surface potentials

Fig. 2 shows the COF and currents as a function of sliding time for a range of applied potentials, with BSA present in the solution from the start of all tests. With a positive potential of +0.5V, the COF was initially noisy, with an average value of ~0.34, Fig. 2Aa. After ~40 min sliding, the COF abruptly dropped to ~0.24 with a remarkably stable friction. There were several brief breakdowns and quick recoveries during the remainder of the test, but otherwise the COF was stable at around 0.24. The current during the test followed the COF very closely, with the two plots looking almost identical, Fig. 2Ba.

When a negative potential -0.5V was applied, after an initial noisy COF, passivation was still observed after about 1.5 hours of sliding. However, there were frequent breakdowns with a noisier COF in the range of 0.28 ~0.32. Breakdowns in the COF were associated with rapid rises and falls in the current, while a stable COF was associated with a stable low current, Fig. 2b.

When a more negative potential of -0.8V was applied, passivation was not observed. The COF was stable around 0.32 but was continuously noisy, but with longer wavelength oscillations. The current followed a roughly similar trend, with the current gradually falling throughout the test, Fig. 2c.

Very similar behaviour was observed with an applied potential of -0.95V (Fig. 2d). Thus, as the applied potential became more negative, a protective layer was less likely formed, resulting in higher, noisier friction. Clearly, a protective tribofilm was formed at OCP and +0.5V and to a lesser extent at -0.5V. As with the -0.8V, the current at -0.9V was largely stable, gradually decreasing throughout the test. Undoubtedly, the surface potential has a major impact on the formation of a protective layer of Ti-6Al-4V in simulated body fluid.

3.1.3. Wear track profile and wear rate

Fig. 3A shows the specific wear rate for the various applied potentials and under OCP conditions comparing the PBS solution on its own with that with the PBS solution and the BSA added. The statistical analysis results from one way ANOVA shows that at the P = 0.05 level, the mean wear rates are significantly different. And the Tukey comparisons test indicates that the difference of the mean wear rates is significant at the 0.05 level. The specific wear rate was the highest when sliding in PBS solution without BSA and lowest in 25% BSA solution with an applied surface potential of +0.5V. The worn surface profiles were similar (other than different wear rates), Fig. 3B, although pile-up was observed at the edge of the wear track at the end of the test with an applied -0.95V. Thus, this provides further evidence that the addition of BSA, which resulted in decreased friction, was associated with the improved formation of a protective tribofilm that resulted in a lower wear rate. Clearly, surface potential influences the formation, or not, of a protective layer, with a protective layer forming at OCP, positive potential, but it does not form at cathodic potentials. The testing time for all the conditions in Fig. 3 was 4.5 hours.

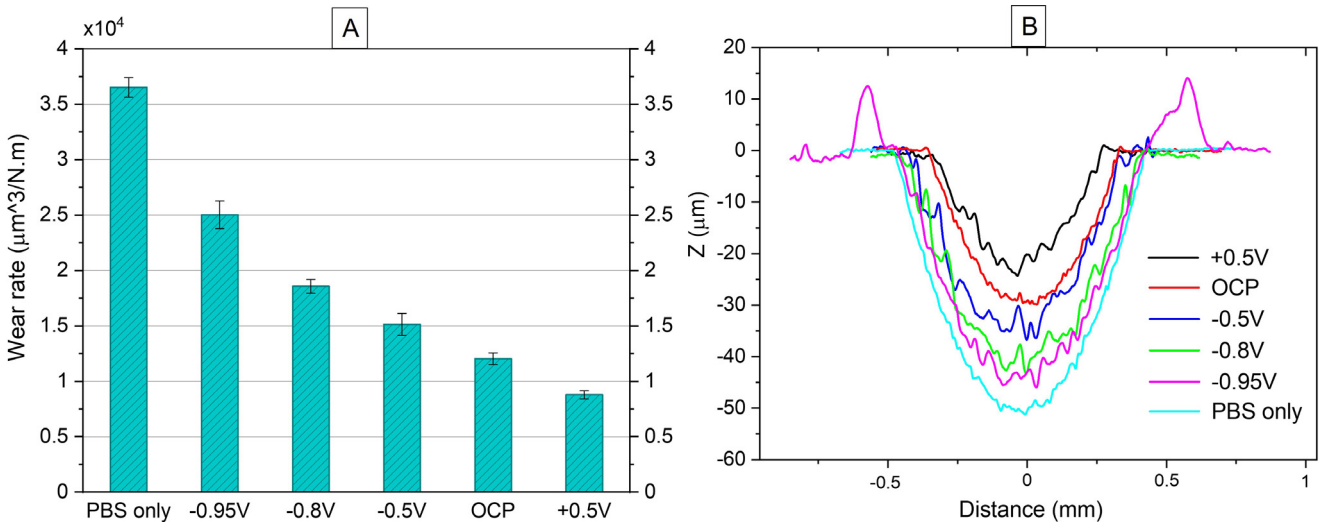

Fig. 3. Comparison of specific wear rate (A) and wear scar profiles (B) for all 4.5h tests at various conditions.

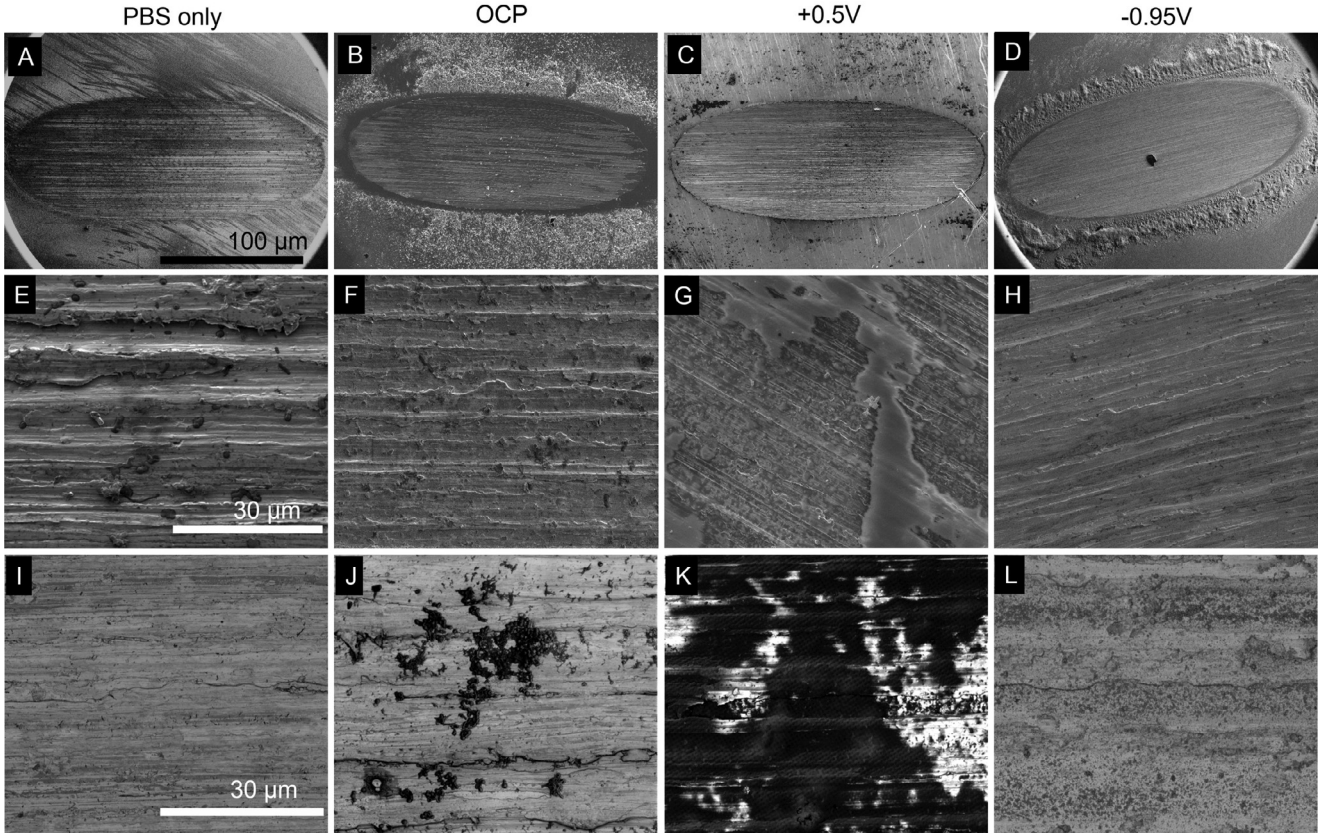

Fig. 4. SE and BC images of plain view of the wear scars from different testing conditions: A) PBS only; B) OCP; C) +0.5V and D) -0.95V. E, F, G, H (SE images) and I, J, K, L (BC images) are the enlarged view of the worn surface, respectively.

3.2. Morphology and chemical composition of the worn surface

Fig. 4 gives low magnification images and details of the worn surfaces for OCP with PBS only, OCP with BSA, +0.5V and -0.95V. Figs. 4a - 4h are secondary electron (SE) images and Figs. 4i - 4l are backscattered electron images. All surfaces showed classic ploughing by the harder alumina counterface asperities. The presence of a tribofilm was apparent in places, e.g. Fig. 4g. Fig. 5 gives a more detailed view of the worn surface morphology and chemical distribution from the tribocorrosion test with +0.5V potential applied after testing for 4.5 hours. The worn surface was characterised by ploughing and cutting. A discontinuous surface layer, with light grey contrast, was present across the grooves and adjacent area, often associated with small debris particles, which showed bright contrast and was rich in sodium and chlorine, suggesting they were salt residues. This intermittent layer is not the adsorbed proteins on the surface since the distribution of potassium does not overlap with this layer. Rather, the layer contained carbon and oxygen. Further evidence from backscattered electron images (Figs. 4j and 4k) shows that the layer on the wear track of the OCP and

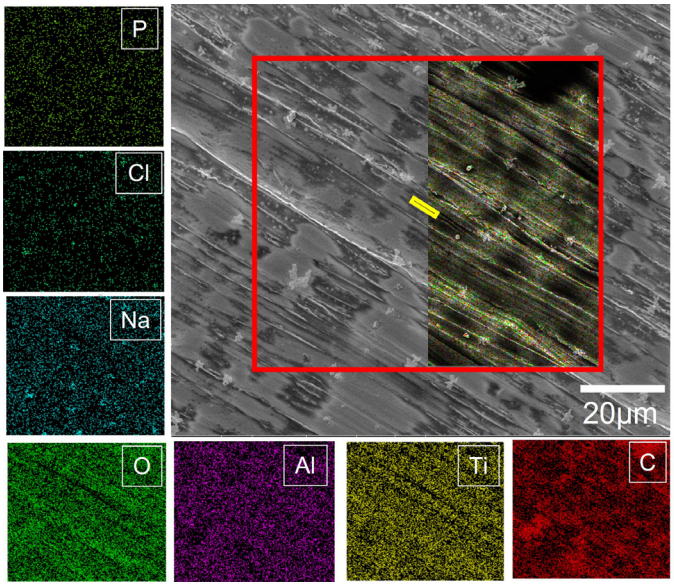

Fig. 5. Wear track morphology and EDX elemental maps of the worn surface after tribocorrosion test with +0.5V potential applied. The yellow rectangular box indicates the sample location of the FIB sample for TEM.

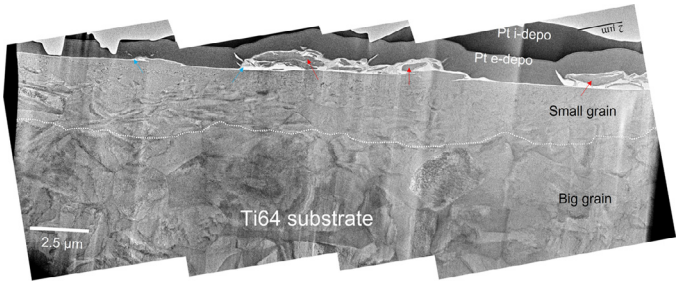

Fig. 6. Bright-field (BF) TEM image shows the cross-section of the +0.5V sample. Presented wear debris (red arrows), tribofilm (yellow arrows), and the subsurface microstructure. Above the dotted white line is the deformed region with fine-grained regions and a nanocrystalline layer, with an abrupt transition to the original substrate. The black box indicates the sample position of Fig. 7.

+0.5V are darker in contrast, which means this layer is probably not only oxides (Figs 4i and 4l). To further investigate this layer and the surface structure, a FIB sample was removed from the region marked by the yellow box in the middle of Fig. 5 for further examination by S/TEM, described in the next section. Similar FIB sections were removed from the samples from other conditions.

3.3. Microstructure and chemical composition of tribofilm and subsurface of the +0.5V sample

Fig. 6 shows an example of a cross-section underneath the worn surface of the +0.5V sample from a region of ~20 × 8 μm. To avoid the damage from the Ga ions during the FIB preparation, two protective Pt deposits were made on top of the surface, firstly by electron deposition and then by ion beam deposition. These layers also served to label the outer worn surface. A complicated surface structure was observed, comprising several different layers from the top to the bottom of the image. Below the Pt deposition, wear debris could be seen attached to the surface (indicated by the red arrows). In addition, a thin tribofilm (bright contrast, indicated by the yellow arrows) was present across the entire surface. The enlarged image of the tribofilm (the black box in Fig. 6) is shown in Fig. 7. A deformed nanocrystalline region was observed between the tribofilm and the white dotted line with a thickness of 2.5 - 3.5 μm. After an abrupt transition, the original microstructure was observed below this.

Fig. 7 gives high resolution STEM high-angle annular dark-field (HAADF) and bright-field (BF) images showing the detailed structure of the wear debris, tribofilm and the nanocrystalline layer on the +0.5V sample. The wear debris (red arrows) had a complex structure comprising a mixture of crystalline and amorphous regions, appearing as an agglomerate of particles with different structures. The crystalline regions appeared to have a similar structure to the nanocrystalline substrate, i.e. containing very fine equiaxed crystallites. The crystalline particles appeared to be wrapped in a layer that exhibited brighter contrast, similar in morphology to the tribofilm and appeared to be predominantly amorphous.

The worn surface itself was covered in a continuous tribofilm, marked by the yellow arrows in Figs. 6 and 7. The tribofilm was continuous, but its thickness varied from place to place in the range of 30 nm to several hundred nm. Closer scrutiny showed that the tribofilm was composed of two distinct layers. The outer layer was very thin (~30 nm) and continuous across the worn surface. The second layer, which was below the outer layer, exhibited darker contrast in bright field images, was much thicker (up to hundreds of nm) and was not continuous across the surface.

Fig. 8 shows the two-layer tribofilm in more detail. High-resolution BF TEM images of the two different layers are shown together with the fast Fourier transforms (FFT) from those images, which is a diffraction pattern of these regions. The outer tribofilm exhibited a typical amorphous structure, as shown by the high-resolution image and FFT shown in Fig. 8C. The layer below this one also exhibited an amorphous like structure, Fig. 8B, but the FFT from this image shows a narrow diffuse diffraction ring which might indicate some short-range order. Although both layers show amorphous structures, there are differences between the two, with the diffuse diffraction halo from the outer layer having smaller atomic spacing over a wider range than the inner layer.

A detailed analysis of the chemical composition of the outer worn surface was conducted. EDX was carried on the outer layers, including the tribofilm and the wear debris, alongside the results from all four testing conditions presented in Fig. S1. The elemental maps suggest the composition of the wear debris and tribofilm are the same, both containing Ti, V, Al, C and O. However, these results are limited by spatial resolution and signal to noise ratio of the technique. Therefore, electron energy loss (EEL) spectra were obtained from each tribofilms and the substrate, Fig. 8. The positions are marked in numbers and colours as 1 (black), 2 (red) and 3 (blue) to the upper layer, lower layer and the substrate, respectively in Fig. 8A, with the resultant EELS spectra shown in Fig. 8D. The outer tribofilm, position 1, is essentially a carbon film, with no Ti or O detected. The carbon K-edge comprises mainly σ^* but with a small π^* peak. This is consistent with the high-resolution image and associated FFT, which shows that this is amorphous carbon. The EEL spectrum from the inner tribofilm, location 2, shows the presence of C, Ti, and a small amount of O. Therefore, the lower part of the tribofilm is a mixture of Ti, C and O. The shape of the C-K edge is similar to that from the outer tribofilm, indicating that the carbon is largely amorphous. The EEL spectrum from the substrate, location 3, is almost only Ti, with very small C and O K-edges, which could be derived from contamination of the TEM specimen. No evidence was found of a discrete continuous oxide film on the surface of the metal.

EELS analysis was also carried out on the wear debris still attached to the surface, shown in Figs. 6 and 7. The results are presented in Fig. S2. Some debris particles exhibited EEL spectra similar to the substrate (position 1 in Fig. S2), i.e. only showing a Ti K-edge. This is consistent with the STEM HAADF image, which suggests that these are metal wear debris fragments. Two spec-

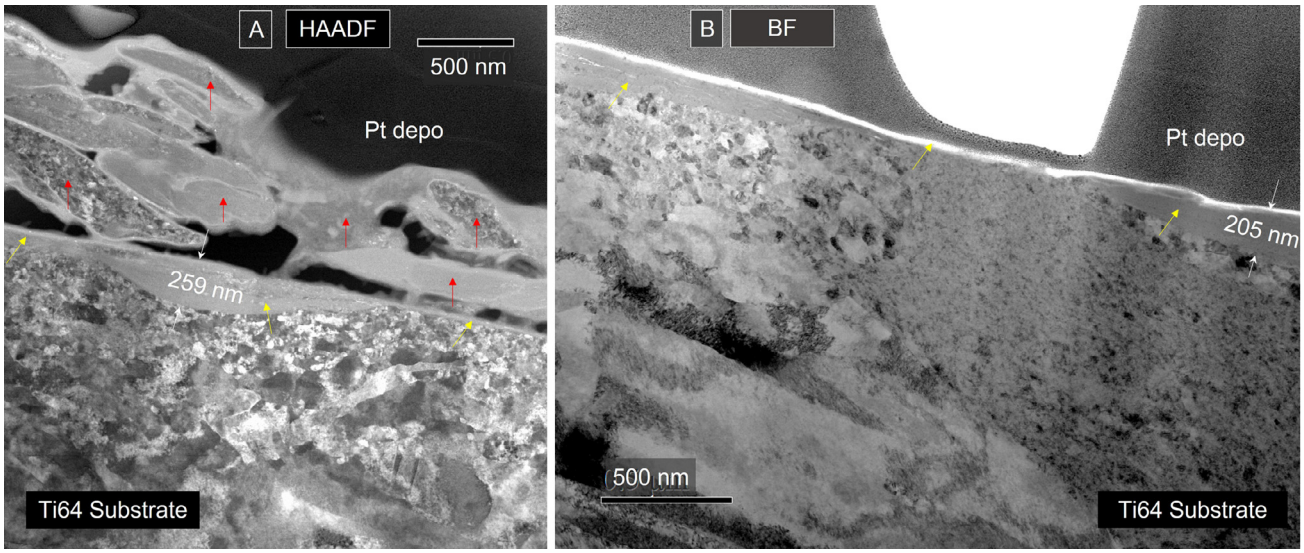

Fig. 7. High magnification STEM images of the surface cross-section of the +0.5V sample. A) HAADF and B) BF images of interface details of debris (red arrows) and tribofilm (yellow arrows), with various thicknesses to a maximum of between 205nm to 259nm.

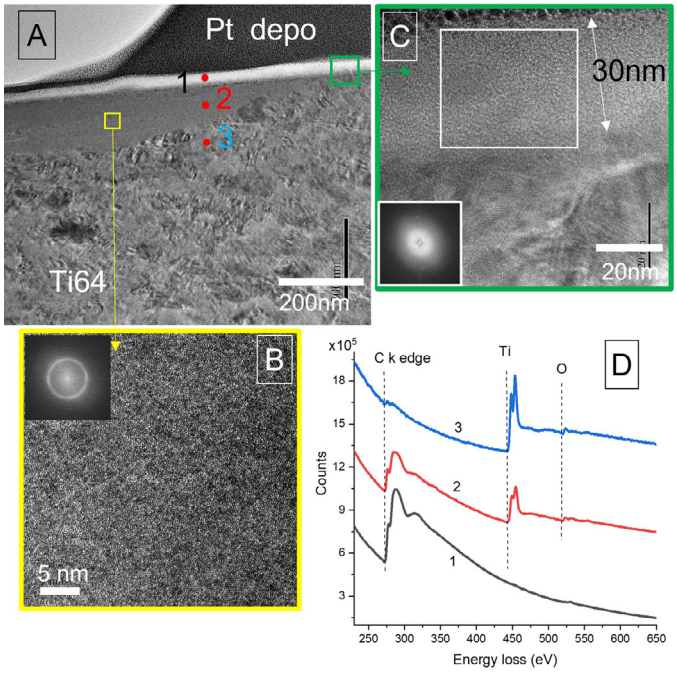

Fig. 8. A) is the enlarged image from the black box in Fig. 6, which shows the detail of the tribofilm. B) and C) are high-resolution images of the yellow and green boxes in A, respectively. The insets in B & C are the corresponding FFT diffractograms for the two layers. D) is an EELS spectrum taken at three positions indicated in A. Position 1 (black) is on the bright upper layer, 2 (red) is on the lower grey layer, and 3 (blue) is on Ti-6Al-4V substrate.

tra were obtained from the carbon-based debris, which exhibited similar contrast to the tribofilm and appeared to wrap around the metallic wear debris or was present as discrete particles. One region, location 2, showed only a C-K edge, but interestingly, the carbon peak exhibited a stronger π^* peak than found in the tribofilm. Another similar region showed a similar C-K edge (again with a stronger π^* peak) but with a small amount of Ti present.

Below the double layer tribofilm, the surface exhibited substantial microstructural changes to the bulk, Fig. 7. Deformation bands containing much finer grains were found running through the surface. The grain size in these bands was similar within a band but different between bands. The crystallite size in these deformation bands was typically 50 nm, but smaller crystallites, which were not easy to resolve, were observed. The interface between these deformation bands and the substrate, and indeed from one deformation band to another, was sharp, with no evidence of microstructural gradation. The deformation bands extended to about 2.5-3μm below the worn surface, at which point there was an abrupt interface with the undeformed substrate.

3.4. Microstructure and chemical composition of the tribofilm and subsurface of the OCP and cathodic samples

Fig. 9 gives cross-sections from the worn surface of the sample tested under OCP conditions in PBS solution, but without a BSA addition. The surface exhibited an intermittent tribofilm that was nearly absent in some regions (Fig. 9A) and extended uniformly up to ~65 nm in other areas (Fig. 9B). High-resolution TEM and FFT analysis of these images showed that the tribofilm was largely amorphous but contained a few crystallites.

The addition of BSA to the PBS solution under OCP conditions resulted in a thicker tribofilm being formed. Fig. 10 shows a representative region, where the variability in the thickness of the tribofilm can be seen, with the thicker regions being about twice as thick (~130 nm) as the PBS solution without BSA. Again, the tribofilm was predominantly amorphous, although a few fine crystallites were present.

BF STEM images from a cross-section of the -0.95V sample are shown in Fig. 11. A relatively uniform but thin (50-70 nm) tribofilm was present. Thus, the tribofilm was nearly an order of magnitude thinner than on the +0.5V sample. The tribofilm was almost entirely amorphous, although again occasional very fine crystallites were present, Fig. 11C.

3.5. Grain size distribution and geometrically necessary dislocation (GND) density characterisation of subsurface

PED was used to characterise the subsurface deformation structures for each test condition. PED allowed the GB and GND density to be measured. GNDs are dislocations with the same Burgers vector sign that accommodate the plastic strain gradients in the microstructure. The GND could be separated for the α-Ti (hcp) and

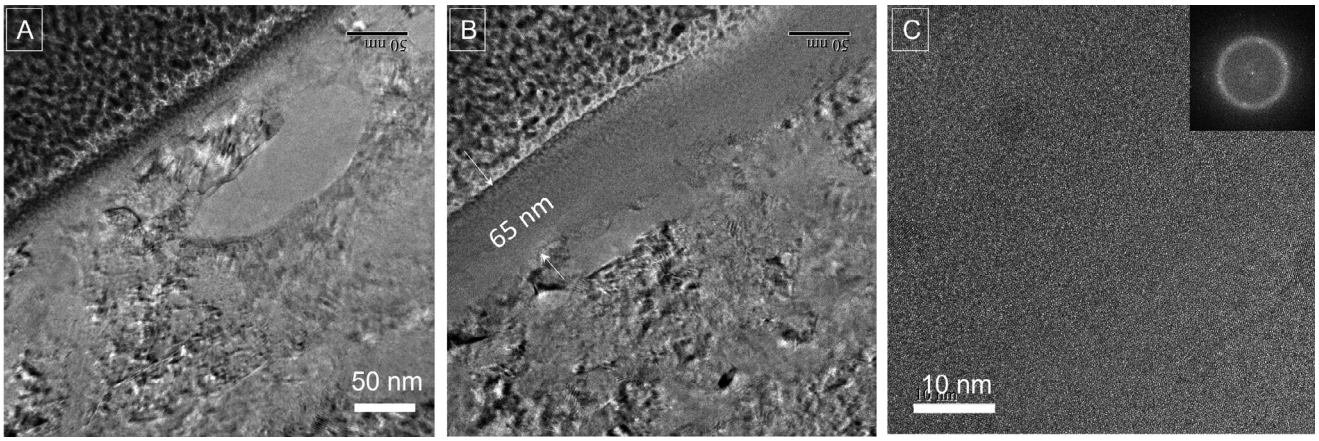

Fig. 9. STEM BF images from a FIB specimen taken from the OCP condition tested in PBS without a BSA addition. A) & B) showing variable thickness tribofilm that was almost absent in some areas (A) and extended up to 65 nm in others (B). C) High-resolution image and insert FFT diffractogram showing the structure of the tribofilm, where present.

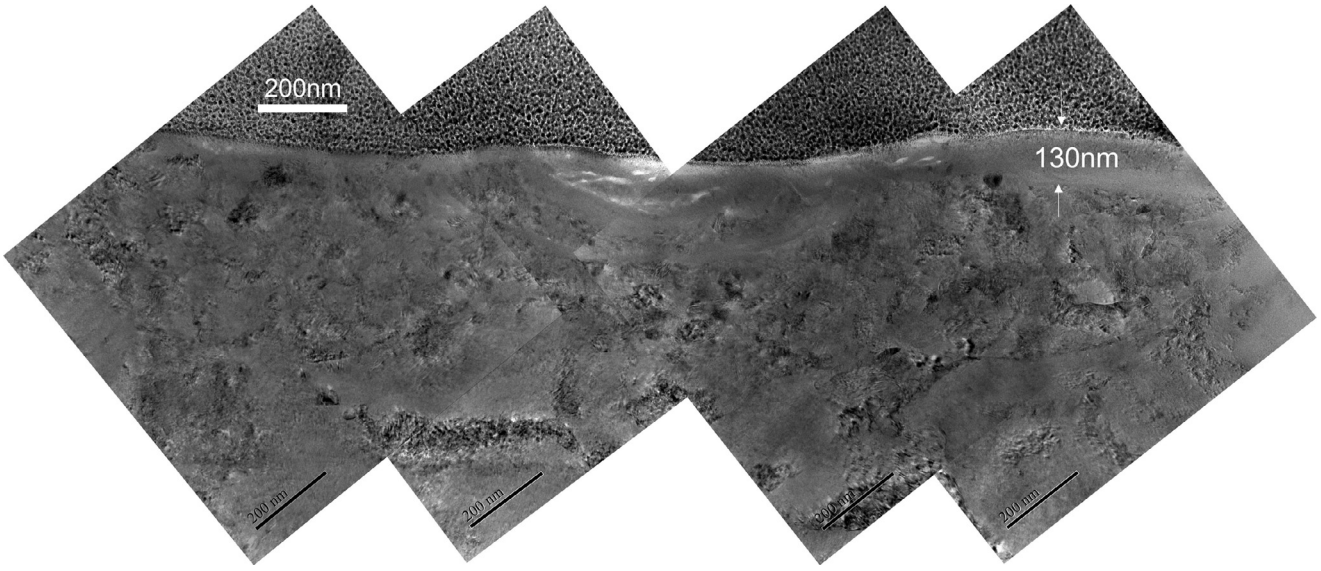

Fig. 10. STEM BF image from a FIB specimen taken from the OCP test after BSA had been added. A tribofilm over variable thickness (up to 130 nm) is present.

β-Ti (bcc) phases. Furthermore, the GND density could be mapped separately for the prismatic and basal slip systems in the hcp α-Ti. The results of this for the various test conditions are summarised in Fig. 12, where $\longleftrightarrow$ indicates the sliding direction and the surface position. The GB positions are superimposed on the GND maps (Fig. 12A). All the grain boundaries are high angle grain boundaries which are $>$ 15 degrees. Some of the grains in the images are blank in all three slip systems. This is because the system could not identify the crystal, which is a result of the structure being amorphous or because the local deformation was so severe that the region could not be indexed. The latter explanation is more likely and was especially obvious seen in the fine grain regions of the +0.5V sample.

The Max Feret Diameter ($FERET_{max}$) was chosen as the parameter to evaluate the grain size. The $FERET_{max}$, also called the caliper diameter, is the largest distance between two parallel tangential lines in any in-plane direction of a grain at an arbitrary angle, illustrated in Fig. 12C. The statistical analysis results (Fig. 12D) show total grain numbers in the region of interest (ROI) are 3622, 1449, 828, 529 for +0.5V, OCP, -0.95V, and PBS_only, respectively. The maximum $FERET_{max}$ are 1020 nm, 2440 nm, 1810 nm, and 290 nm for +0.5V, OCP, -0.95V, and PBS_only, respectively. The Kruskal-Wallis ANOVA method shows at p = 0.01 level that each test condition's grain size distribution is significantly different for one and the other. Dunn's test shows that the difference of the means is significant at P = 0.05 level. Except for the PBS_only, the other three samples have a comparable region. The +0.5V has the largest number of grains and about 81% of which are under 20 nm. The +0.95V has the smallest grain number in the three tests, and 58% falls in the 30 – 40nm range.

The statistical analysis results from the Kruskal-Wallis ANOVA show that at the P = 0.01 level, the GND density distributions calculated for the four samples are significantly different for all three selected slip systems. Dunn's test shows that at P = 0.05 level, the difference of the means is significant. The data were summarised and presented by the histograms in Fig. 12B. In the HCP basal and prismatic slip systems, the +0.5V sample has the highest GND density at and above 1×10^{16}. The +0.5V sample also has the highest GND density at and above 1×10^{15} in the β-BCC slip system.

In all samples, the dislocation density was far greater in the nanocrystalline region than in the other regions. Moreover, the dislocation density was much higher in the α-phase (hcp) than in the β-phase (bcc). The β-titanium was often broken into small fragments by the deformation process. In addition, the GND density

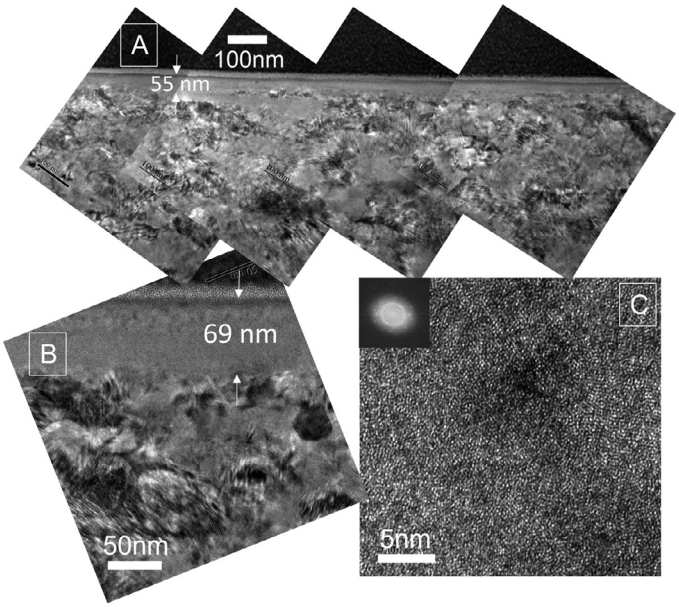

Fig. 11. STEM BF images from a FIB sample from the test at -0.95V. A uniform tribofilm is present with various thicknesses from 50-70nm, A) & B). It was a single layer tribofilm, B). C) High-resolution image of the tribofilm, which has the appearance of a mechanically mixed layer, comprising a mixture of amorphous and crystalline material.

was higher on hcp basal planes than on the prismatic planes across all four samples.

The GND density was a strong function of the test condition. The -0.95V exhibited the lowest GND density, while the +0.5V had the highest GND density for all the slip systems. The GND density in the OCP test in the PBS solution without BSA was similar to those obtained in the -0.95V. The GND density in the OCP test with BSA was smaller than that of +0.5V. The extent of the nanocrystalline layer, broadly defined as having a grain size of less than 50 nm, was much greater for the +0.5V sample compared with all the other conditions, as previously shown in Fig. 7. Indeed, the nanocrystalline surface layer was only fully developed under the +0.5V conditions.

3.6. Structure and chemical composition of wear debris in the test solution

Wear debris in the testing solution after tribocorrosion experiments were collected for TEM investigation. TEM images of the typical remains found in the solution are presented in Fig. S3 for the specimen tested at +0.5V. The same features were found in the solutions from OCP and -0.5V tests.

The particles/fragments had a layered or sheet-like morphology, with two sheets often seen together but also smaller rounder-shaped particles, Fig. S3. These particles comprised Ti, Al and/or V oxides, presumably formed during the tribo-corrosion process. A carbon layer of variable thicknesses surrounded these particles (note that the particles were suspended on a silicon substrate to ensure that any carbon detected had only come from the sample and not the sample preparation).

Further investigation of these surrounding sheets demonstrated that the thicker ones were often amorphous. The thin ones are more likely a mixture of different carbon structures. Some parts were amorphous, and some parts had a regular long-range ordered arrangement. In some regions, a graphitic structure or even graphene-like flakes were found, Fig. 13A. The high-resolution TEM image shows the characteristic honeycomb 2D structure with the distances between the atoms 0.141nm, and the lattice spacing 0.25 nm (Fig. 13B), which agrees with the length of the σ-bond and lattice vector in graphene 2D hexagonal lattice (inset in Fig. 13A), respectively [35].

Other carbon allotrope structures, such as nanocarbon onion, were found in the test solutions from ±0.5V and OCP samples (Fig. 14). Nanocarbon onions, also called onion-like carbon or carbon nano-onions (CNO), are nanoscopic carbon particles with a nearly spherical shape of multiple enclosed fullerene-like carbon shells [37].

Fig. 14A are the EELS spectra of the onion-like structure. The corresponding positions are indicated in Fig. 14B, a HAADF image from the +0.5V 1h sample. EELS spectra and measured spacing (approximate 0.34 - 0.35 nm) confirm this to be onion-like carbon. The carbon K-edge contained a small p* peak, associated with the graphitic type bonding. When compared with the carbon K-edge fine structure (ELNES) spectra of carbon onions formations from Feng et al. [38] and the Maroc et al. [37], the CNO found in our test solution were still in the middle stages of formation and have not fully complete. Oxygen is also detected in the EELS spectra. Moreover, close examination indicates a very small N K-edge. The presence of N and O K-edges suggests the source of where the CNO evolved from, which is the BSA protein initially in the system.

Fig. 14C is a TEM image from the +0.5V 4.5h sample. The CNOs are marked by orange arrows and amorphous carbon indicated by red arrows on the same sheet, surrounding metal oxide particles, as noted before. This confirms that the film that covers the oxides is a mixture of different carbon structures. Figs. 14D and E are the TEM images of CNO from OCP and -0.5V samples, respectively. The spacing between two neighbouring layers and the size of the diffuse halo shows the dominant spacing is approximate ~0.35 nm.

4. Discussion

4.1. The role that protein plays in the tribofilm formation

What happens at a contacting surface is a rather complicated combination of several processes, including the mechanical wear process, the corrosion processes, the role of liberated debris, the absorption effects such as the attachment of oligomers and the decomposition of proteins, with whatever product results from that.

The tests run under OCP conditions without a protein addition, followed by the addition of a protein, were designed to investigate the role that protein plays in the tribocorrosion process. The addition of protein (BSA) certainly improved the tribocorrosion behaviour as the COF decreased and the variation in COF became much less, which coincided with passivation (Fig. 1). This was associated with a slight improvement in the wear rate. It implies that a protective layer was formed on the surface, with the protein an integral part of the formation process, which was confirmed by TEM, as discussed below.

BSA has several isomeric forms at different pH. In addition, how the protein absorbs will depend on the applied potential. At a neutral pH, BSA is in the normal form (N-form, also known as heart-shaped form) and carries a net negative charge with the most compact conformation [16,39,40]. Beykal et al. [40] reported that the adsorption of negatively charged BSA to gold surfaces under a range of constant applied voltage (+ 0.5V to - 0.5V) at pH = 6.78. It was observed that adsorption occurred under all conditions but with different total mass adsorption and adsorption rate. The greatest mass adsorption and rate occurred at +0.5V, and the lowest adsorption and rate was at -0.5V. Moreover, Park et al. [15] reported that temperature-induced denatured BSA oligomers in bulk solution adsorbed more quickly and in larger mass quantities onto silica surfaces. When BSA monomers were thermally denatured (30 min at 70 °C) they had irreversible conformational changes from N-form to an extended form (E-form) and assem-

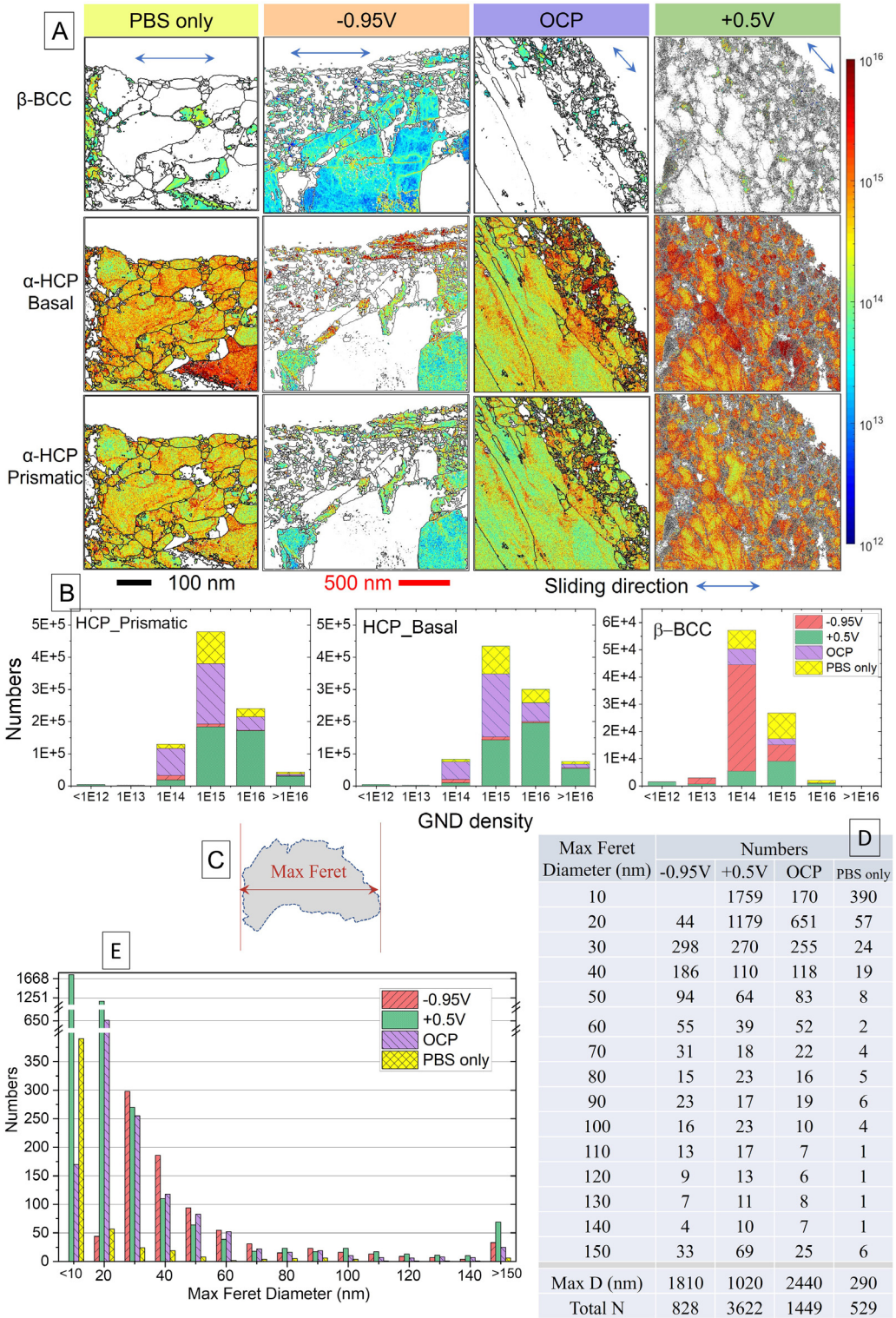

Max Feret Diameter (nm)	Numbers			
	-0.95V	+0.5V	OCP	PBS only
10		1759	170	390
20	44	1179	651	57
30	298	270	255	24
40	186	110	118	19
50	94	64	83	8
60	55	39	52	2
70	31	18	22	4
80	15	23	16	5
90	23	17	19	6
100	16	23	10	4
110	13	17	7	1
120	9	13	6	1
130	7	11	8	1
140	4	10	7	1
150	33	69	25	6
Max D (nm)	1810	1020	2440	290
Total N	828	3622	1449	529

Fig. 12. GB and GND results. A) GB superimposed on the GND density distribution maps in the subsurface regions from the four selected testing conditions. The scale bar is 100 nm on the PBS sample and is 500 nm for the remaining three samples. The colour scale is log(GND density in m^2). Arrows indicate the sliding direction and surface position. B) Histograms for GND density distribution at three selected slip systems. C) Schematic illustration of Max. Feret Diameter, D) Calculated grain size (max ferret diameter) chart, and E) Histogram of the grain size distribution for each testing condition.

bled into more adhesive oligomers with much larger surface contact area and remained stable. As a result, the oligomers serve as a superior passivation agent to inhibit biofouling on a silica surface. The pH of the simulated body-fluid used in this study was around 7 during testing, but the surface in our case is Ti-6Al-4V which has different surface chemistry from gold and silica surfaces. However, the absorption of BSA onto a Ti alloy surface under different electrochemical conditions has been reported and exhibits similar behaviour [14]. The protein behaviour and the solution chemistry should be comparable, and therefore it is reasonable to deduce

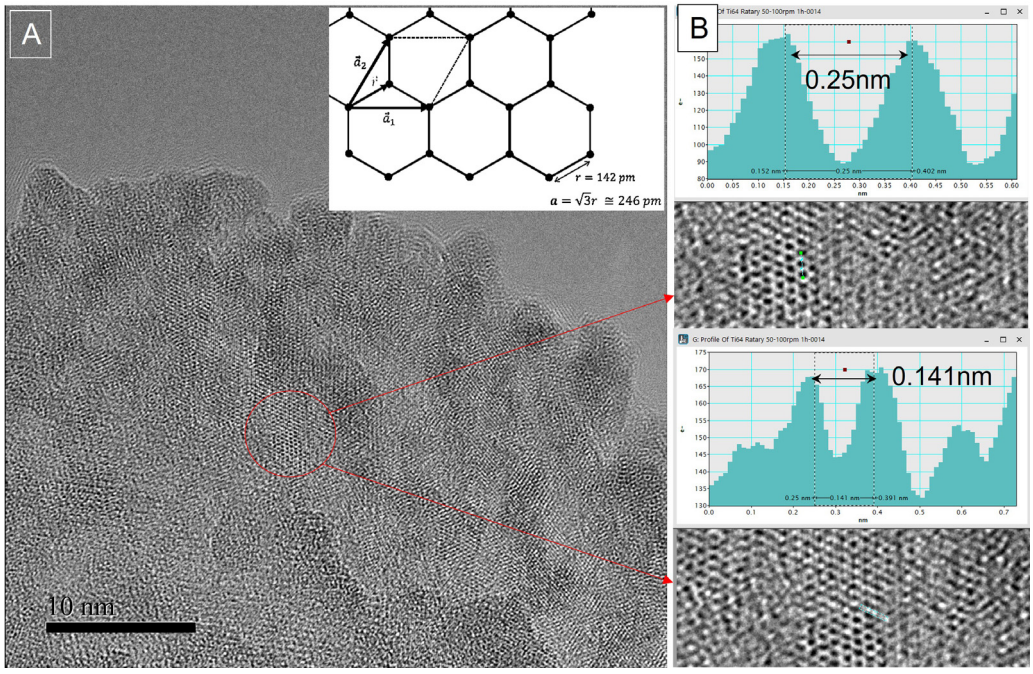

Fig. 13. High-resolution TEM image A) showing the graphic-like structure found on the thin film around the particles from the test solution of the +0.5V sample. The inset is the schematic real space hexagonal lattice with a 2-atom base with parameters [36]. B) Measured lengths between atoms and enlarged image of the red circle in A.

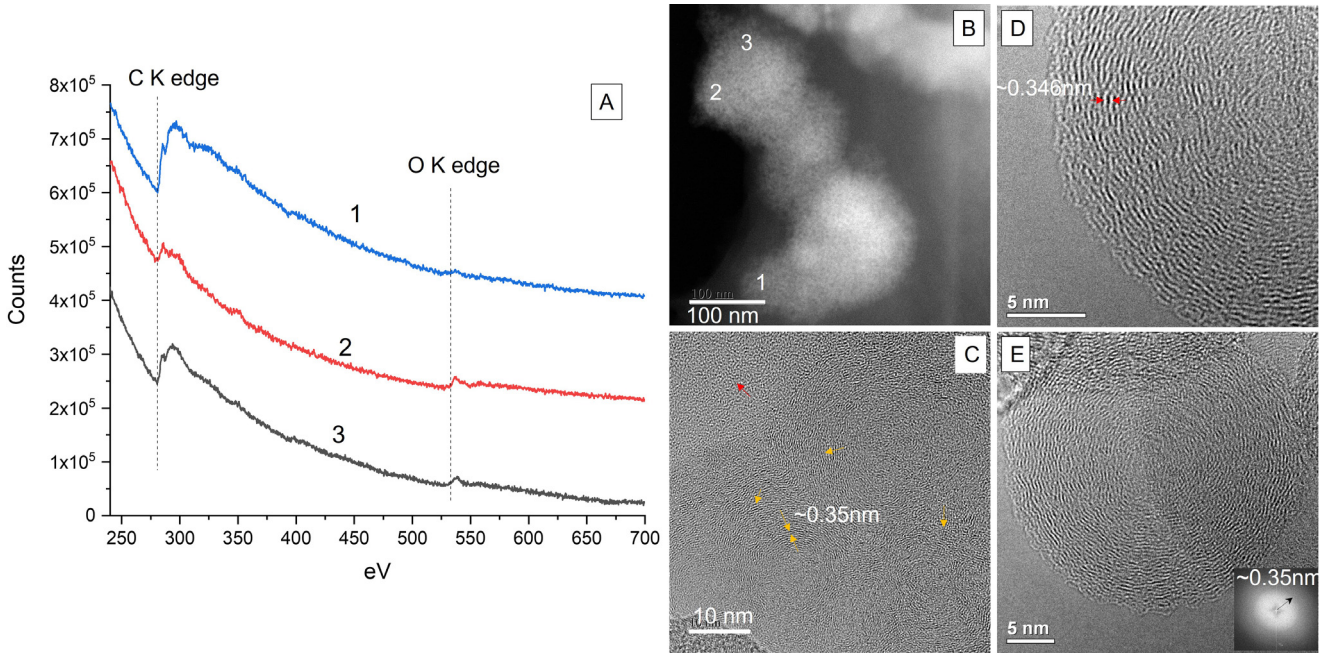

Fig. 14. Carbon onion structure found in testing solutions under various conditions: A) EELS spectra of onion-like structure and the positions are indicated in B; B) HADDF image from +0.5V 1h sample; and C) TEM image from +0.5V 4.5h sample. Carbon onion (orange arrow) and amorphous (red arrow) on a sheet around particles; D) TEM image from OCP sample; E) TEM image from -0.5V sample. The inset is the FFT diffractogram for the structure shows the dominant spacing is ~0.35nm.

that similar processes would take place in our system. Hence, the BSA molecules will have carried a net negative charge and be attracted to the surface with the greatest mass and fastest rate at +0.5V and the lowest mass and the slowest rate at -0.95V. After the addition of BSA proteins, monomers are attracted and attached to the surface but are repeatedly removed by the wear process. The heat generated by friction between the surfaces will raise the temperature around the contact area which in turn will denature the protein monomers and then induce the irreversible conversion of monomers to oligomers. However, as discussed later, the flash temperature rise was considered to be relatively small in these experiments. This results in better coverage and passivation on the surface. This process takes a while which is why in Fig. 1 the COF dropped a bit immediately with the addition of BSA, and then after ~40 minutes, it became smooth associated with the brief rise in the OCP. The initially formed protective layer was quickly broken down until ~15 minutes later a much more stable and adhesive protective layer formed.

4.2. The structure of the wear debris

In the current work, a careful analysis of the wear debris was undertaken after it was extracted from the lubricant. Nanocarbon structures, including CNO, were observed in the wear debris from the OCP and ±0.5V tests, Figs. 13, 14. This is not the first time that CNO have been observed, with Liang et al. reporting CNOs in the wear debris removed from a tribofilm on explanted CoCrMo femoral heads [22]. Nanocarbon materials have been widely studied and used in various applications, including the tribology industry, since they exhibit excellent lubrication properties [41,42]. CNO was first found by Ijima [43] as a by-product while looking at a sample of carbon black in a TEM. Since then, various approaches have been taken to prepare CNO, as reviewed by Zeiger et al. [37], and most of the methods require extreme conditions such as high temperature (>1800°C), or high pressure, or both to obtain high yield and quality under an inert atmosphere. Other synthesis methods were reported to produce CNO, such as by decomposing of carbon-containing precursors, for instance, methane [44], naphthalene [45], lycopene extracted from tomatoes [46], ghee oil [47] etc., where it is possible to form CNO at relatively low temperatures (200 - 600 °C) without the presence of metal catalysts. Obviously, the degradation process that the BSA proteins undergo in the current tests is far more than a simple denaturation in that the primary structure of the protein is not affected [48]. Although there is no direct research on this process, it is rational to presume that protein could be the carbon-containing precursor and decomposed to form CNO structures found in this work.

In the current work, the solution temperature was kept constant at around 37 °C, but of course, friction induced temperature transients could potentially increased temperature, albeit for short time periods. A comprehensive summary of the available methods for the calculation of flash temperature for various contact geometries is given in ref. [49]. All calculations require a knowledge of the asperity contact radius, i.e. the true contact area. Using what might be considered relatively severe contact conditions, the flash temperature rise is calculated to be no more than 20 °C. This is consistent with other published calculations, for example, Bos measured a flash temperature rise of 64°C for much more severe conditions than those used here (0.23m/s, 400N compared to 0.02m/s and 0.5N) [50].

In addition to the local temperature rises, the local contact stresses could potentially have contributed to CNO formation. While the initial nominal Hertzian contact stress was ~600 MPa, this will have been amplified at the asperity contacts to an extent dependent on the true area of contact, exceeding the yield stress of the material. Moreover, the breakdown of the passive film at contacting asperities will have led to locally high current densities. For example, for the 0.5V test, the observed current was a maximum of ~75μA (Fig. 2B). This corresponds to a current density of ~7.5mA cm^{-2} over the apparent contact area (as measured from the traces in Fig. 3B). The true area of contact will have been much smaller than the apparent area of contact, although the surfaces were examined after running in, where conformal contact will have resulted. The current density at a contacting asperity that results in breaching the passive layer will have been substantially higher than ~7.5mA cm^{-2}, but not high enough in itself to lead to the formation of the CNO structures, which requires ~100A cm^{-2} (as described below). Thus, it must have been the combination of temperature transients, high local contact pressure and high local current density as the passive film is breached that led to the formation of CNOs.

There may be a concern that the CNO structures were an artefact of electron irradiation during S/TEM experiments. Ugarte [51] observed the transformation tendency of carbon soot to form multiple shell spheres ('onions') under intense electron-beam irradiation in a 300 keV high-resolution electron microscope. The conditions under which carbon onions formed under the electron beam are electron energies above 100 keV, beam intensities of the order of 100 A cm^{-2} and irradiation times of several minutes for the transformation of polyhedral to spherical onions up to hours for the transformation of amorphous carbon to onions [52]. In the current study, extreme caution was exerted during S/TEM observation. Under the normal operating condition, the dose was carefully controlled around 10 A•cm^{-2}, i.e. an order of magnitude below that at which electron-induced onion structures are formed. Moreover, the silicon monoxide support film used to prepare wear debris from the lubricating solution is very sensitive to dose and will break down when the current density is higher than the normal operating condition. The operating conditions used here did not result in any degradation of the silicon monoxide support film. Thus, we are confident that the CNOs did not arise from damage induced by the electron beam.

A question arises as to why no CNO structures or any other highly order carbon structures were observed in the tribofilms (Figs. 7–10), but were a frequent observation in the wear debris retrieved from the lubricating serum. This was not an error in sampling statistics as many worn surfaces were studied and in no case was a CNO structure found. Differences in the structure of wear debris and the worn surface structure are quite common [53]. These observations imply that structural changes occur during the formation of wear debris particles. It was the combination of the locally high contact pressure at an asperity, the local flash temperature from frictional heating and the locally high current density associated with the breaching of the passive film that resulted in the formation of CNO structures as the wear debris particle is formed. Only the amorphous carbon formed from degraded proteins which were attracted and attached to the contact surface has been left on the surface and formed the more stable and protective layer, which improved the friction performance at the same time.

4.3. The formation of the tribofilm as a function of potential

High-resolution S/TEM observations of FIB specimens removed from the worn surface of all test conditions showed that the tribofilm was predominantly amorphous, Figs 8–11, but in some regions it contained metallic wear debris (Fig. 7). At +0.5V, the tribofilm had two layers, an outer layer that was entirely amorphous and an inner layer that contained small amounts of crystalline material that appeared to be titanium or titanium oxide based (Figs. 7, 8). This inner tribofilm is almost certainly the product of the synergic effects of mechanical mixing and corrosion processes. The EELS spectra taken from the +0.5V condition showed that the carbon K edge was predominantly σ^* with a smaller π^* peak. Interestingly, the debris attached to the worn surface, Fig. S2, exhibited a stronger π^* peak than found in the tribofilm. However, the shape of the carbon K-edge was still consistent with graphitic bonding and is almost identical to that reported by Liao et al. [22] for a tribofilm scrapped off a retrieved CoCrMo femoral head. Similar observations of graphitic bonding in tribofilms have been observed by various authors for several different materials, including metals such as CoCrMo [18,54], carbon-based coatings [55,56] and ceramics [57].

The thickness and extent of coverage of the tribofilm depended strongly on the surface potential. The tribofilm at +0.5V was ~200 – 260 nm and a double layer (containing amorphous carbon and some nanocrystalline fragments, Fig. 8). For the anodic conditions, more CNO was produced on both the surface and in the solution adjacent to the wear track than under other conditions. At OCP, the tribofilm was variable, up to ~130 nm. At -0.95V, the tribofilm was again of variable thickness but was the thinnest (up to ~69 nm) of all conditions where BSA was present. Thus, the precise role of the

BSA molecules depended on the surface potential. As noted earlier, since the BSA molecules will have carried a net negative charge, more protein oligomers will be attracted to the surface at the anodic potential of +0.5V, and the lowest mass and slowest rate at the cathodic potential of -0.95V, consistent with the thickness of the tribofilm formed.

It is interesting to note that a classical continuous oxide film was not found under OCP or anodic conditions. The STEM techniques used here certainly had sufficient resolution to locate a discrete oxide film, although such films can be extremely thin, for example, Zeng et al. [23] observed a film of just 2nm on the surface of a CoCrMo alloy in a similar solution to the one used here. Thus, the view that depassivation events seen in Fig. 2B were a result of breaching of the oxide film cannot be supported in the current work. Rather, the experimental evidence is that depassivation was associated with removal of the tribofilm, as discussed below, exposing bare metal, which is a much larger event than the removal of a few nm of oxide.

Tribofilm comprises predominantly amorphous carbon, with significant amounts of titanium and smaller amounts of oxygen. Some parts of the tribofilm contain metallic wear debris that has a similar structure to the nanocrystalline layer. This observation and the incorporation titanium into the tribofilm suggests a mechanical mixing mechanism between the protein and the heavily deformed titanium. Indeed, the transition from nanocrystalline metal to the amorphous structure can been seen in Fig. 7 in several places; in some the metal crystallites are still clearly visible while in others the fine (nm) remnants of the crystalline structure can be seen in predominantly amorphous areas (as shown by the FFT in Fig. 8C).

Thus, the process of tribofilm formation appears to have been driven by firstly the proteins being attracted to the surface with the greatest mass and fastest rate at +0.5V. This was then mechanically mixed with the nanocrystalline surface metal, which was more extensive at +0.5V. The tribofilm was responsible for surface passivation, with the removal of the tribofilm (and not a discrete oxide film) resulting in depassivation.

4.4. The role of tribofilm and surface structure on friction and wear

The tribofilm had a clear effect on the friction. The friction tended to be lower and the friction coefficient less noisy for the anodic potential test compared to the cathodic potential tests, Fig. 2. Thus, friction was lower and with less noise for the thicker tribofilms and wider coverage. This is consistent with the graphitic bonding in the tribofilm that imparts lubricating properties of the tribofilm. Moreover, the current during the test followed the COF very closely, with the two plots looking almost identical, Fig. 2B. Thus, this gives direct evidence that the formation of the tribofilm led to passivation of the surface.

The wear rates observed were a function of the surface potential, Fig. 3, and therefore the extent of formation of a tribofilm. The highest wear rate was associated with the absence of BSA under OCP conditions. The reduction in wear rate from the addition of BSA, with the associated increase in tribofilm coverage and thickness clearly demonstrates that the absorption of proteins onto a surface reduces the wear rate. The next highest wear rate was associated with cathodic conditions of -0.95V, with the lowest wear rate under anodic conditions of +0.5V. Thus, the wear rate correlated with the thickness and coverage of the tribofilm, with the lowest wear rates coming from the thickest tribofilm. This result is consistent with that of Namus et al. [58], who found that the lowest wear rate for CoCrMo alloys as a function of the load was associated with the formation of a tribofilm, whereas the highest wear rate was associated with no tribofilm. Similarly, Gispert et al. [59] found that albumin absorption resulted in the lowest wear rates for metallic surfaces when sliding against ultra-high molecular weight polyethene. As shown by Namus et al. [58] and Wimmer et al. [60], the formation of a tribofilm is load-dependent, with a minimum load required for film formation.

The reciprocating contact resulted in plastic deformation of the worn surface, the extent of which depended strongly on surface potential, Figs. 6, 7, 10, 12. The deformed structure was characterised by measuring the GND density using PED for the first time, which gives a quantitative measure of the damage accumulation. The -0.95V exhibited the lowest GND density, with only limited deformation observed. The GND density in the PBS solution without BSA was similar to that obtained in the -0.95V and the OCP test with BSA tests. In contrast, the +0.5V had the highest GND density, measured in both hcp and bcc phases and each slip system in the hcp phase. A clear nanocrystalline layer was developed in the surface region of the +0.5V sample, broadly defined as having a grain size of less than 50 nm, which was not clearly developed in the other conditions. The hardness and modulus of the material of this nanocrystalline layer were greater than the other surfaces (Fig. 10).

Perret et al. [20] have observed a similar effect of potential on the extent of surface strain and the formation of a nanocrystalline layer for 304L stainless steel, with similar trends to those observed here. The absence of a passive film led to a low dislocation density, while anodic conditions led to an extensive, thick, nanocrystalline layer. In both the present tests and those of Perret et al. [20], the friction coefficient was 0.3 or above, so the maximum shear stress would have been at the surface. In the current work, the friction was the lowest for the anodic conditions and so friction-induced deformation would have been the least in this case. In any event, differences in friction between tests were small and so this could not explain differences in the extent of the nanocrystalline layer. Perret et al. [20] argue that the passive film present under anodic conditions, which was associated with the thickest nanocrystalline layer, will have prevented dislocation annihilation at the surface, leading to greater accumulated strain. However, in the current work, no descrete continuous oxide film was found on the surface, rather the tribofilm itself provided the surface passivation.

In contrast to the anodic conditions, under cathodic conditions, dislocations would be attracted to the surface and thus be annihilated. This remains the most plausible explanation for the differences observed. However, it is difficult to envisage how the differences in surface dislocation trapping or annihilation can lead to the differences in a nanocrystalline layer being absent in one case but present to a thickness of at least 1μm in the other. Future work is required to fully understand the correlation between strain accumulation and surface potential.

The wear rates decreased in the order PBS without BSA under OCP (highest), -0.95V through to +0.5V (lowest wear rate). Thus, the wear rate decreased as the thickness and coverage of the tribofilm increased. Equally, the wear rate decreased as the surface strain accumulation increased. A higher surface strain was associated with a higher surface hardness, but correlations of hardness with wear are notoriously difficult. The manner in which the nanocrystalline layer affects the wear rate is complex. Namus et al. [61] compared the tribocorrosion behaviour of CoCrMo alloys in which a nanocrystalline structure had been deliberately induced in the material, which was then compared to the normal undeformed surface. A marginal improvement in wear rate was found for the nanocrystalline structure, but this gain was offset by the much greater corrosion contribution to wear arising from the nanocrystalline structure. Similarly, Namus et al. [58] examined the load-dependent wear transition in CoCrMo alloys. They found that the thickest nanocrystalline layer was associated with the post wear rate transition, where the wear rates were an order of magnitude higher than that of the pre-transition condition, for which

only a minimal nanocrystalline layer was present. Moreover, the nanocrystalline layer had substantially higher hardness than the starting surface, but this clearly did not lead to reduced wear. A more likely explanation is that the tribofilm on the surface was directly responsible for reducing the wear rate in a way it effectively reduced the material loss due to corrosion (Figs. 1 and 2). As a result, the small (< 50 nm) nanocrystalline structure survives when a thicker tribofilm covers the surface (Fig. 12). What was observed in the current study is consistent with the observations of Wimmer [60], who found minimum wear rates with the most developed tribofilm.

5. Conclusions

In this study, commercially available alloy Ti-6Al-4V has been tested in simulated body fluid at different surface potentials. The role of protein in the lubricant was also explored by investigating PBS solution without a BSA addition under OCP conditions.

The formation of a tribofilm on the surface strongly depended on the applied potential and on the presence of protein. The tribofilm was largely absent when the PBS solution did not contain protein under OCP conditions. This led to the highest friction and wear rate. The addition of protein under the same conditions led to the more widespread formation of a tribofilm and a reduction in both friction and wear rate.

The tribofilm coverage and thickness depended on the applied potential. It was the thinnest and the least coverage under cathodic conditions, while it was the thickest under anodic conditions. The tribofilm was carbon-based and exhibited graphitic bonding in all cases. Under cathodic conditions, the tribofilm had a two-layer structure, with an outer layer comprising amorphous carbon with graphitic bonding and an inner layer that was similar but contained nanocrystals derived from the titanium substrate. The wear rate decreased with the thickness and extent of coverage of the tribofilm.

The finding of nanocarbon onion in test solutions (±0.5V and OCP) fills one of the missing links in the formation of tribofilm. These structures were not found in the tribofilm on the worn surface itself. It is believed that they form under high pressures under a contacting asperity during wear debris formation.

Under the protection of the extra thick tribo-film on the worn surface, the anodically charged sample had the largest nanocrystalline region with high GND density and a grain size <50nm, which led to increased hardness and modulus. However, it was not believed that there was a correlation between wear rate and the thickness/properties of the deformed surface.

Author contributions

JQ conceptualised the idea, designed and conducted the experiments, wrote the original draft. WMR provided supervision, validation, writing, review & editing. JN contributed to the PET data collecting and processing and discussion. DG contributed to the GND data calculation and discussion. BW contributed to statistical analysis, editing MATLAB scripts, calculating and extracting the GND data from the maps. All authors reviewed the manuscript.

Data availability statement

The raw and processed data required to reproduce these findings are available to download from Qi, Jiahui (2021), “Ti64 CNO”, Mendeley Data, V1, doi:10.17632/bm2b9nm923.1.

Declaration of Competing Interest

The authors declare that they have no known competing financial interests or personal relationships that could have appeared to influence the work reported in this paper.

Acknowledgement

This work is supported by the Engineering and Physical Sciences Research Council (grant number EP/001766/1) as a part of ‘Friction: The Tribology Enigma’ Programme Grant (www.friction.org.uk), a collaboration between the Universities of Leeds and Sheffield.

The authors wish to acknowledge the Henry Royce Institute for Advanced Materials, funded through EPSRC grants EP/R00661X/1, EP/S019367/1, EP/P02470X/1 and EP/P025285/1, for access to the JEOL JEM-F200 and the Bruker Tribolab through Royce@Sheffield.

DG would like to thank the UKRI MRC for his Future Leaders Fellowship, MR/T019123/1.

The authors wish to acknowledge Dr J. Zhu and the Leonardo Centre for Tribology and Surface Science, The University of Sheffield for accessing Alicona.

Supplementary materials

Supplementary material associated with this article can be found, in the online version, at doi:10.1016/j.actbio.2022.01.027.

References

[1] V. Migonney, Biomaterials, John Wiley & Sons, Inc., Hoboken, NJ, USA, 2014.
[2] D.M. Brunette, P. Tengvall, M. Textor, P. Thomsen (Eds.), Titanium in Medicine, Springer-Verlag, Berlin Heidelberg, 2001.
[3] T. Wachi, T. Shuto, Y. Shinohara, Y. Matono, S. Makihira, Release of titanium ions from an implant surface and their effect on cytokine production related to alveolar bone resorption, Toxicology 327 (2015) 1–9.
[4] J.L. Gilbert, Corrosion in the human body: metallic implants in the complex body environment, Corrosion 73 (12) (2017) 1478–1495.
[5] D.R. Bijukumar, A. Segus, J.C.M. Souza, X. Li, M. Barba, L.G. Mercuri, J.J. Jacobs, M.T. Mathew, Systemic and local toxicity of metal debris released from hip prostheses: a review of experimental approaches, Nanomed. Nanotechnol., Biol. Med. 14 (3) (Apr. 2018) 951–963.
[6] P.F. Doorn, P.A. Campbell, J. Worrall, P.D. Benya, H.A. McKellop, H.C. Amstutz, Metal wear particle characterization from metal on metal total hip replacements: transmission electron microscopy study of periprosthetic tissues and isolated particles, J. Biomed. Mater. Res. 42 (1) (Oct. 1998) 103–111.
[7] E. Ingham, J. Fisher, Biological reactions to wear debris in total joint replacement, Proc. Inst. Mech. Eng. Part H J. Eng. Med. 214 (1) (Jan. 2000) 21–37.
[8] K.T. Kim, M.Y. Eo, T.T.H. Nguyen, S.M. Kim, General review of titanium toxicity, Int. J. Implant Dent. 5 (1) (Dec. 2019) 10.
[9] C. Fonseca, M.A. Barbosa, Corrosion behaviour of titanium in biofluids containing H2O2 studied by electrochemical impedance spectroscopy, Corros. Sci. 43 (3) (2001) 547–559.
[10] F. Kaiser, D. Scharnweber, S. Bierbaum, C. Wolf-Brandstetter, Success and side effects of different treatment options in the low current attack of bacterial biofilms on titanium implants, Bioelectrochemistry 133 (2020) 107485.
[11] V. Swaminathan, J.L. Gilbert, Fretting corrosion of CoCrMo and Ti6Al4V interfaces, Biomaterials 33 (22) (2012) 5487–5503.
[12] M.T. Mathew, J.J. Jacobs, M.A. Wimmer, Wear-corrosion synergism in a CoCrMo hip bearing alloy is influenced by proteins, Clin. Orthop. Relat. Res. 470 (11) (Nov. 2012) 3109–3117.
[13] R. Namus, J. Nutter, J. Qi, W.M. Rainforth, The influence of protein concentration, temperature and cathodic polarization on the surface status of CoCrMo biomedical grade alloys, Appl. Surf. Sci. 499 (Jan. 2020) 143908.
[14] D.R. Jackson, S. Omanovic, S.G. Roscoe, Electrochemical studies of the adsorption behavior of serum proteins on titanium, Langmuir 16 (12) (Jun. 2000) 5449–5457.
[15] J.H. Park, J.A. Jackman, A.R. Ferhan, G.J. Ma, B.K. Yoon, N.J. Cho, Temperature-induced denaturation of BSA protein molecules for improved surface passivation coatings, ACS Appl. Mater. Interfaces 10 (38) (2018) 32047–32057.
[16] B. Jachimska, A. Pajor, Physico-chemical characterization of bovine serum albumin in solution and as deposited on surfaces, Bioelectrochemistry 87 (2012) 138–146.
[17] D.H. Tsai, F.W. Delrio, A.M. Keene, K.M. Tyner, R.I. MacCuspie, T.J. Cho, M.R. Zachariah, V.A. Hackley, Adsorption and conformation of serum albumin protein on gold nanoparticles investigated using dimensional measurements and in situ spectroscopic methods, Langmuir 27 (6) (2011) 2464–2477.

[18] W.M. Rainforth, P. Zeng, L. Ma, A.N. Valdez, T. Stewart, Dynamic surface microstructural changes during tribological contact that determine the wear behaviour of hip prostheses: metals and ceramics, Faraday Discuss 156 (2012) 41.
[19] M.A. Wimmer, A. Fischer, R. Buscher, R. Pourzal, C. Sprecher, R. Hauert, J.J. Jacobs, Wear mechanisms in metal-on-metal bearings: the importance of tribochemical reaction layers, J. Orthop. Res. 28 (4) (2010) 436–443.
[20] J. Perret, E. Boehm-Courjault, M. Cantonic, S. Mischlera, A. Beaudouind, W. Chittyd, J.-P. Vernotd, EBSD, SEM and FIB characterisation of subsurface deformation during tribocorrosion of stainless steel in sulphuric acid, Wear 269 (5–6) (2010) 383–393.
[21] S.Guadalupe Maldonado, S. Mischler, M. Cantoni, W.J. Chitty, C. Falcand, D. Hertz, Mechanical and chemical mechanisms in the tribocorrosion of a Stellite type alloy, Wear 308 (1–2) (2013) 213–221.
[22] Y. Liao, R. Pourzal, M.A. Wimmer, J.J. Jacobs, A. Fischer, L.D. Marks, Graphitic tribological layers in metal-on-metal hip replacements, Science (80-.). 334 (6063) (Dec. 2011) 1687–1690.
[23] P. Zeng, A. Rana, R. Thompson, W. Rainforth, Subsurface characterisation of wear on mechanically polished and electro-polished biomedical grade CoCrMo, Wear 332–333 (May 2015) 650–661.
[24] J. Hesketh, M. Ward, D. Dowson, A. Neville, The composition of tribofilms produced on metal-on-metal hip bearings, Biomaterials 35 (7) (Feb. 2014) 2113–2119.
[25] S. Balachandran, Z. Zachariah, A. Fischer, D. Mayweg, M.A. Wimmer, D. Raabe, M. Herbig, Atomic scale origin of metal ion release from hip implant taper junctions, Adv. Sci. 7 (5) (Mar. 2020) 1903008.
[26] M.A. Wimmer, A. Fischer, R. Büscher, R. Pourzal, C. Sprecher, R. Hauert, J.J. Jacobs, Wear mechanisms in metal-on-metal bearings: the importance of tribochemical reaction layers, J. Orthop. Res. 28 (4) (2009) n/a-n/a.
[27] I. Ghamarian, P. Samimi, Y. Liu, B. Poorganji, V.K. Vasudevan, P.C. Collins, Characterizing the nano-structure and defect structure of nano-scaled non-ferrous structural alloys, Mater. Charact. 113 (2016) 222–231.
[28] X. Liu, Y. Zhou, X. Zhu, D. Wang, Q. Fan, The failure mechanism at adiabatic shear bands of titanium alloy: high-precision survey using precession electron diffraction and geometrically necessary dislocation density calculation, Mater. Sci. Eng. A 746 (Feb. 2019) 322–331.
[29] I. Ghamarian, Y. Liu, P. Samimi, P.C. Collins, Development and application of a novel precession electron diffraction technique to quantify and map deformation structures in highly deformed materials—as applied to ultrafine-grained titanium, Acta Mater. 79 (August) (Oct. 2014) 203–215.
[30] I. Ghamarian, P. Samimi, A. Telang, V.K. Vasudevan, P.C. Collins, Characterization of the near-surface nanocrystalline microstructure of ultrasonically treated Ti-6Al-4V using ASTAR™/precession electron diffraction technique, Mater. Sci. Eng. A 688 (November 2016) (2017) 524–531.
[31] R. Namus and W. M. Rainforth, "The influence of cathodic potentials on the surface oxide layer status and tribocorrosion behaviour of CoCrMo and Ti6Al4V alloys in simulated body fluid," Unpublished results, 2021.
[32] R.W.W. Hsu, C.C. Yang, C.A. Huang, Y.S. Chen, Investigation on the corrosion behavior of Ti-6Al-4V implant alloy by electrochemical techniques, Mater. Chem. Phys. 86 (2–3) (2004) 269–278.
[33] F. Bachmann, R. Hielscher, H. Schaeben, Grain detection from 2d and 3d EBSD data—specification of the MTEX algorithm, Ultramicroscopy 111 (12) (Dec. 2011) 1720–1733.
[34] A. Mavraki, P.M. Cann, Friction and lubricant film thickness measurements on simulated synovial fluids, Proc. Inst. Mech. Eng. Part J J. Eng. Tribol. 223 (3) (2009) 325–335.
[35] A.H. Castro Neto, F. Guinea, N.M.R. Peres, K.S. Novoselov, A.K. Geim, The electronic properties of graphene, Rev. Mod. Phys. 81 (1) (Jan. 2009) 109–162.
[36] Alexandre Faia Carvalho, "Simultaneous synthesis of diamond on graphene for electronic applications," Universidade de Aveiro.
[37] M. Zeiger, N. Jäckel, V.N. Mochalin, V. Presser, Review: Carbon onions for electrochemical energy storage, J. Mater. Chem. A 4 (9) (2016) 3172–3196.
[38] Z. Feng, Y. Lin, C. Tian, H. Hu, D. Su, Combined study of the ground and excited states in the transformation of nanodiamonds into carbon onions by electron energy-loss spectroscopy, Sci. Rep. 9 (1) (Dec. 2019) 3784.
[39] Ronald P.Taylor, Enzyme-like activities associated with albumin, in: Albumin: Structure, Function and Uses, 1977, pp. 183–201.
[40] B. Beykal, M. Herzberg, Y. Oren, M.S. Mauter, Influence of surface charge on the rate, extent, and structure of adsorbed Bovine Serum Albumin to gold electrodes, J. Colloid Interface Sci. 460 (2015) 321–328.
[41] N. Luo, J.X. Xiang, T. Shen, H.L. Liang, S. Xin, One-step gas-liquid detonation synthesis of carbon nano-onions and their tribological performance as lubricant additives, Diam. Relat. Mater. 97 (June) (2019) 107448.
[42] L. Joly-Pottuz, N. Matsumoto, H. Kinoshita, B. Vacher, M. Belin, G. Montagnac, J.M. Martin, N. Ohmae, Diamond-derived carbon onions as lubricant additives, Tribol. Int. 41 (2) (2008) 69–78.
[43] S. Iijima, Direct observation of the tetrahedral bonding in graphitized carbon black by, J. Cryst. Growth 50 (1980) 675–683.
[44] C. He, N. Zhao, C. Shi, X. Du, J. Li, Carbon nanotubes and onions from methane decomposition using Ni/Al catalysts, Mater. Chem. Phys. 97 (1) (2006) 109–115.
[45] M. Choucair, J.A. Stride, The gram-scale synthesis of carbon onions, Carbon N. Y. 50 (3) (2012) 1109–1115.
[46] V. Singh, Natural source derived carbon nano-onions as electrode material for sensing applications, Diam. Relat. Mater. 87 (June) (2018) 202–207.
[47] T.H. Mongwe, B.J. Matsoso, B.K. Mutuma, N.J. Coville, M.S. Maubane, Synthesis of chain-like carbon nano-onions by a flame assisted pyrolysis technique using different collecting plates, Diam. Relat. Mater. 90 (September) (2018) 135–143.
[48] C. Molnar, J. Gair, Biological molecules, Conceptes in Biology, 2012.
[49] Francis E Kennedy, Frictional heating and contact temperatures, in: B. Bushan (Ed.), Modern Tribology Handbook, Volume 1, Principles of Tribology, CRC Press, 2001.
[50] J. Bos, Frictional Heating of Tribological Contacts PhD Thesis, University of Twente, 1995.
[51] D. Ugarte, Curling and closure of graphitic networks under electron-beam irradiation, Nature 359 (6397) (1992) 707–709.
[52] Florian Banhart, Irradiation effects in carbon nanostructures nanostructures, Rep. Prog. Phys. Irradiat. 62 (8) (1999).
[53] Z. Zhou, W.M. Rainforth, C.C. Tan, P. Zeng, J. Ojeda, M. Romero-Ganzalez, P.Eh. Hovsepian, The role of the tribofilm and roll-like debris in the wear of nanoscale nitride PVD coatings, Wear 263 (7-12 SPEC. ISS) (2007) 1328–1334.
[54] P. Zeng, A. Rana, R. Thompson, W.M. Rainforth, Subsurface characterisation of wear on mechanically polished and electro-polished biomedical grade CoCrMo, Wear 332–333 (2015) 650–661.
[55] Z. Zhou, I.M. Ross, L. Ma, W.M. Rainforth, A.P. Ehiasarian, P. Hovsepian, Wear of hydrogen free C/Cr PVD coating against Al2O3 at room temperature, Wear 271 (9–10) (2011) 2150–2156.
[56] I.C. Müller, J. Sharp, W.M. Rainforth, P. Hovsepian, A. Ehiasarian, Tribological response and characterization of Mo–W doped DLC coating, Wear 376–377 (2017) 1622–1629.
[57] P. Zeng, W.M. Rainforth, T.D. Stewart, Characterisation of the wear mechanisms in retrieved alumina-on-alumina total hip replacements, Wear 376–377 (2017) 212–222.
[58] R. Namus, P. Zeng, W.M. Rainforth, Correlation of the wear transition in CoCrMo alloys with the formation of a nanocrystalline surface layer and a proteinaceous surface film, Wear 376–377 (2017) 223–231.
[59] M.P. Gispert, A.P. Serro, R. Colaço, B. Saramago, Friction and wear mechanisms in hip prosthesis: comparison of joint materials behaviour in several lubricants, Wear 260 (1–2) (2006) 149–158.
[60] M.A. Wimmer, M.P. Laurent, M.T. Mathew, C. Nagelli, Y. Liao, L.D. Marks, J.J. Jacobs, A. Fischer, The effect of contact load on CoCrMo wear and the formation and retention of tribofilms, Wear 332–333 (2015) 643–649.
[61] R. Namus, W.M. Rainforth, Y. Huang, T.G. Langdon, Effect of grain size and crystallographic structure on the corrosion and tribocorrosion behaviour of a CoCrMo biomedical grade alloy in simulated body fluid, Wear 478–479 (October 2020) (2021) 203884.